HYBRID SOLUTION TO FLUID FLOW IN IRREGULAR MICROCHANNELS GENERATED BY FABRICATION IMPERFECTIONS

Isabela Florindo Pinheiro, isabelaflorindo@gmail.com
Leandro Alcoforado Sphaier, lasphaier@id.uff.br

Laboratory of Thermal Sciences (LATERMO), Department of Mechanical Engineering (PGMEC), Universidade Federal Fluminense (UFF). Rua Passo da Pátria, 156 Bl. E sala 206-D, Niterói, Rio de Janeiro, Brazil

Abstract: *As microfluidics began to emerge as a revolutionary field, new manufacturing approaches became needed for the fabrication of advanced microchannel devices. Nevertheless, depending on the micro-fabrication employed, the resulting geometry may present variations from the designed one, due to fabrication issues. In this context, an investigation is carried out to determine the two-dimensional velocity profile for fully developed laminar flow in nominally rectangular microchannel, considering three different cross-section imperfections: inclined walls, rounded corners and a slightly curved surface. A hybrid numerical-analytical solution is employed based on the Generalized Integral Transform Technique to solve the problem in the considered irregular geometry and the effects of each imperfection on the velocity profile is examined.*

Keywords: *Microchannels, Imperfections, Micro-fabrication, GITT*

1. NOMENCLATURE

$A_{m,n}$	transformed equation coefficients
$B_{m,n}$	transformed equation coefficients
F	filter
N	norm
p	pressure
u	velocity
T	modified dimensionless velocity
U	dimensionless velocity
$\bar{u}$	average velocity
x, y	spatial coordinates
Greek symbols	
β	eigenvalues
ϕ	trapezoid angle
φ	dimensionless upper boundary position
μ	dynamic viscosity
ρ	fluid density or specific mass
ξ, η	dimensionless coordinates
θ	filtered potential
$\bar{\theta}$	transformed potentials
Y	eigenfunctions
Dimensionless parameters	
Γ	dimensionless pressure gradient
K	aspect ratio
Subscripts	
n, m	summation indexes
$n_{\max}$	truncation order

2. INTRODUCTION

The introduction of micro-technologies such as Microelectromechanical Systems (MEMS) and Microfluidics Devices only became possible with the development of new techniques in the Microfabrication area. Among various currently available microfabrication techniques (Abate *et al.*, 2009; Kovacs *et al.*, 1998; Petersen, 1982), many can involve imperfections, such as dimensional errors, surface roughness, rounded corners, and problems in straightness. Although small irregularities may not be disclosed by manufacturers of commercially-available rectangular micro-channels, they can affect the velocity profile and hence interfere in the designed microfluidics applications. Florindo *et al.* (2015) investigated the influence of the effects of fabrication imperfections in nominally-rectangular micro-channels on the fully developed velocity profile. A hybrid analytical-numerical solution was employed for a trapezoidal-like geometry, and the results were compared with the experimental work presented by Puccetti *et al.* (2014).

In the literature, many studies presented analytical solutions to laminar flows in rectangular channels (Aparecido and Cotta, 1990; Chalhub and Sphaier, 2010; Lindquist and Aparecido, 1999; Shokouhmand and Jomeh, 2007). However, when trapezoidal cross-sections are considered, numerical methods are required (Cao *et al.*, 2005; McHale and Garimella, 2010; Qu *et al.*, 2000; Sheikhalipour *et al.*, 2009; Niazmand *et al.*, 2008). Some experimental studies related to water flows in trapezoidal microchannels can also be mentioned (Wu and Cheng, 2003; Weilin *et al.*, 2000).

In order to overcome the limitation offered by an exclusive analytical model and to offer an alternative method of solution unlike traditional numerical methods, the Generalized Integral Transformed Technique (GITT) (Cotta, 1993), is used to acquire the hybrid analytical-numerical solution needed. Some works that employ this technique to micro-channel applications can be mentioned. The investigation by Knupp *et al.* (2013) proposed a single domain formulation of conjugated conduction-convection heat transfer problems in micro-channels, extending the single domain formulation for conjugate conduction-convection problems presented previously in Knupp *et al.* (2012), by taking into account the axial diffusion effects. Sphaier (2012) used the hybrid methodology to analyze a Graetz-type problem in parallel-plates micro-channels with the combination of electroosmotic and pressure driven flows with isothermal walls. Also, the work of Naveira-Cotta *et al.* (2010) employed an inverse analysis to the problem of forced convection with slip-flow.

This paper presents itself as an extension of the work proposed in Florindo *et al.* (2015), which compares the calculated results with experimental data of Puccetti *et al.* (2014). In both investigations, the authors found a discrepancy between the experimental velocity profile and the theoretical predictions obtained by considering a square cross-section. The results revealed a higher error in areas closer to the micro-channel walls. This was explained later by a two-dimensional view of the micro-channel cross-section using a SEM image, revealing that the micro-channel were actually trapezoidal with rounded corners and curved surface. The purpose of this paper is to refine the conclusions obtained by previous studies with an analytical-numerical model that provides a closer velocity profile to experimental data in Puccetti *et al.* (2014).

3. MATHEMATICAL FORMULATION

From figure 1, a microchannel cross-section is depicted as a trapezoidal-like geometry with imperfections characterized by rounded corners and slightly curved surface. The edges on the upper boundary of the trapezoidal cross-section are

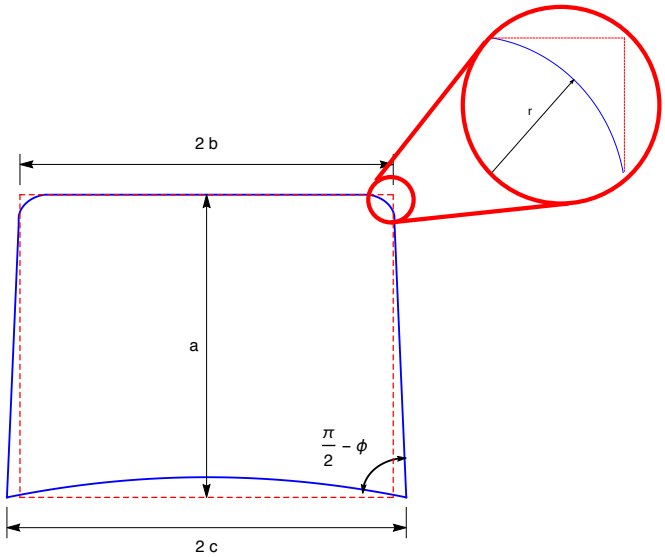

Figure 1: **Approximated Micro-channel Cross-section.**

approximated by a section of a circle with radius r, and the wall on the lower boundary is a convex surface with a height difference of h from the perfect shape.

The mathematical formulation for the steady incompressible laminar flow inside this imperfect micro-channel is based

on a dynamically developed flow. Then, the problem formulation is represented by the governing equations below:

$$\frac{\partial^2 u}{\partial x^2} + \frac{\partial^2 u}{\partial y^2} = \frac{1}{\mu}\frac{\mathrm{d}p}{\mathrm{d}z} \quad \text{for} \quad 0 \leq x \leq a, \quad y_0(x) \leq y \leq y_1(x) \tag{1a}$$

$$\left(\frac{\partial u}{\partial x}\right)_{x=0} = u(c,y) = 0, \quad \text{for} \quad y_0(x) \leq y \leq y_1(x), \tag{1b}$$

$$u(x, y_0(x)) = u(x, y_1(x)) = 0, \quad \text{for} \quad 0 \leq x \leq c, \tag{1c}$$

The lower and upper boundary equations are described below by $y_0(x)$ and $y_1(x)$, respectively.

$$y_0(x) = h - A_1\, x^2 \tag{2a}$$

$$y_1(x) = \begin{cases} a, & \text{if} \quad 0 \leq x < x_1 \\ \sqrt{r^2 - (x - r_x)^2} + r_y, & \text{if} \quad x_1 \leq x \leq x_2 \\ \frac{a\,c}{c-b} - \cot(\phi)\, x, & \text{if} \quad x_2 < x \leq c \end{cases} \tag{2b}$$

The function characterized by $y_1(x)$ within $x_1 \leq x \leq x_2$ is representative of the circumference equation with radius r and center r_x, r_y.

3.1 Normalization

The normalization process is based on a set of dimensionless quantities, which are introduced in the governing equation and boundary conditions:

$$U(\xi,\eta) = \frac{u}{\bar{u}} \quad , \qquad \eta = \frac{y}{a} \quad , \qquad \xi = \frac{x}{c} \tag{3}$$

Based on the previous dimensionless parameters, the normalized problem formulation is described by:

$$\gamma^2 \frac{\partial^2 U}{\partial \xi^2} + \frac{\partial^2 U}{\partial \eta^2} = -\Gamma, \quad \text{for} \quad 0 \leq \xi \leq 1, \quad \varphi_0(\xi) \leq \eta \leq \varphi_1(\xi), \tag{4a}$$

$$\left(\frac{\partial U}{\partial \xi}\right)_{\xi=0} = U(1,\eta) = 0, \quad \text{for} \quad \varphi_0(\xi) \leq \eta \leq \varphi_1(\xi), \tag{4b}$$

$$U(\xi, \varphi_0(\xi)) = U(\xi, \varphi_1(\xi)) = 0, \quad \text{for} \quad 0 \leq \xi \leq 1, \tag{4c}$$

The dimensionless pressure gradient Γ, the rectangular aspect ratio K and the parameter γ are written as:

$$K = \frac{a}{b} \qquad \Gamma = -\frac{a^2}{\bar{u}}\frac{1}{\mu}\frac{\mathrm{d}p}{\mathrm{d}z}, \qquad \gamma = \frac{a}{c} = \frac{K}{1 + K\,\tan(\phi)}, \tag{5}$$

As the limits defined by the domain are normalized, the upper and lower boundaries $y_1(x)$ and $y_0(x)$ are now represented by $\varphi_1(\xi)$ and $\varphi_0(\xi)$, respectively. The current normalized model are depicted in figure 2 and the normalized equations for $\varphi_1(\xi)$ and $\varphi_0(\xi)$ can be analysed in equations 6 e 7.

$$\varphi_0(\xi) = \frac{y_0}{a} = \delta - \Omega_1 \xi^2 \tag{6}$$

$$\varphi_1(\xi) = \begin{cases} 1, & \text{if} \quad 0 \leq \xi \leq \xi_1 \\ \sqrt{\rho^2 - (\xi - r_\xi)^2} + r_\eta, & \text{if} \quad \xi_1 \leq \xi \leq \xi_2 \\ \frac{1}{\gamma\,\tan(\phi)}\,(1 - \xi), & \text{if} \quad \xi_2 \leq \xi \leq 1 \end{cases} \tag{7}$$

The normalized circumference equation is now represented by a radius ρ and center r_ξ, r_η. Also, the geometric

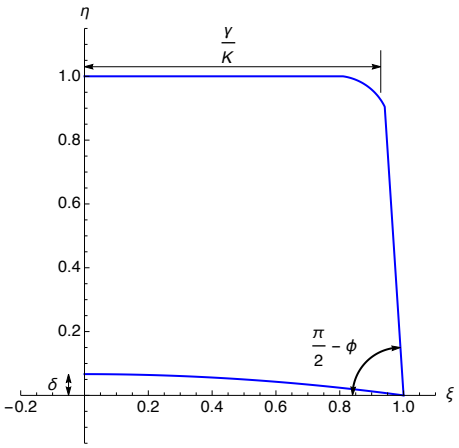

Figure 2: **Normalized Domain.**

parameters that defines the height of the convex lower boundary and the rounded edges are now represented by δ and ρ.

After the process of normalization, a variable transformation is introduced:

$$\Psi(\xi,\eta) \;=\; \Gamma\, U(\xi,\eta) \tag{8}$$

With the variable transformation in equation (8), the pressure gradient Γ is eliminated from the normalized equation, gaining a new transformed PDE system:

$$\gamma^2\,\frac{\partial^2\Psi}{\partial\xi^2}+\frac{\partial^2\Psi}{\partial\eta^2}=-1, \tag{9a}$$

$$\left(\frac{\partial\Psi}{\partial\xi}\right)_{\xi=0} \;=\; \Psi(1,\eta) \;=\; 0, \tag{9b}$$

$$\Psi(\xi,\varphi_0(\xi)) \;=\; \Psi(\xi,\varphi_1(\xi)) \;=\; 0, \tag{9c}$$

In order to calculate the value of the dimensionless pressure gradient Γ, it must be guaranteed that the dimensionless velocity is normalized with the cross-section average velocity, as follows:

$$\Gamma \;=\; \int_0^1\int_{\varphi_0}^{\varphi_1}\Psi\,\mathrm{d}\eta\,\mathrm{d}\xi \tag{10}$$

The dimensionless pressure gradient is numerically calculated for the imperfect trapezoidal cross-section. Another way to evaluate the pressure gradient with the geometric parameters of the analysed geometry is through the Poiseuille Number, as depicted below:

$$\mathrm{Po} = f\,\mathrm{Re} = 2\,\Gamma\left(\frac{D_H}{a}\right)^2 \tag{11}$$

4. SOLUTION SEPARATION PROCESS

The solution separation is introduced in order to improve the convergence and the development of the solution for the problem at hand. The solution $\Psi(\xi,\eta)$ is then separated into a two-dimensional filter $F(\xi,\eta)$ and a filtered variable $\psi(\xi,\eta)$, as can be seen below:

$$\Psi(\xi,\eta) \;=\; \psi(\xi,\eta)+F(\xi,\eta) \tag{12}$$

The solution separation is commonly applied in diffusion problems when the differential equation and the boundary conditions are not homogeneous.

A restriction on $F(\xi,\eta)$ is that it must satisfy the same homogeneous boundary conditions as the original problem for

$\Psi(\xi,\eta)$, such that $\psi(\xi,\eta)$ will also obey the same boundary conditions:

$$\gamma^2\,\frac{\partial^2\psi}{\partial\xi^2}+\frac{\partial^2\psi}{\partial\eta^2}=-(1+G(\xi,\eta)), \tag{13a}$$

$$\left(\frac{\partial\psi}{\partial\xi}\right)_{\xi=0}=\psi(1,\eta)=0, \tag{13b}$$

$$\psi(\xi,\varphi_0(\xi))=\psi(\xi,\varphi_1(\xi))=0, \tag{13c}$$

The two-dimensional problem that represents the filter $G(\xi,\eta)$ is described as below:

$$G(\xi,\eta)=\gamma^2\,\frac{\partial^2 F}{\partial\xi^2}+\frac{\partial^2 F}{\partial\eta^2} \tag{13d}$$

5. INTEGRAL TRANSFORM SOLUTION

Through the Generalized Integral Transform Technique (Cotta, 1993), the hybrid solution of the considered problem is obtained. As first step of the procedure to apply the **GITT**, the Transform-Inverse pair is defined:

$$\text{Transform} \quad\Longrightarrow\quad \overline{\psi}_m(\xi)=\int_{\varphi_0}^{\varphi_1}\psi(\xi,\,\eta)Y_m(\eta;\xi)\,\mathrm{d}\eta, \tag{14a}$$

$$\text{Inverse} \quad\Longrightarrow\quad \psi(\xi,\,\eta)=\sum_{m=1}^{\infty}\frac{\overline{\psi}_m(\xi)\,Y_m(\eta;\xi)}{N_m}, \tag{14b}$$

where Y_m's are orthogonal solutions of a Sturm-Liouville problem.
The Eigenvalue Problem is calculated based on the one-dimensional Helmholtz problem, as portrayed below:

$$Y_m''(\eta)+\beta_m^2\,Y_m(\eta)=0,\qquad \text{for}\qquad \varphi_0(\xi)\le\eta\le\varphi_1(\xi), \tag{15a}$$

$$Y_m(\varphi_0(\xi))=0,\qquad Y_m(\varphi_1(\xi))=0. \tag{15b}$$

Unlike simpler cases of two-dimensional problems, the eigenfunctions rely not only on the dimensionless coordinate η, but with the dimensionless coordinate ξ as well, with the notation $Y_m(\eta;\xi)$ used to indicate that Y_m depends on ξ as a parameter. This approach is directly linked by the selection of a imperfect trapezoidal-like domain. The solution for the Eigenvalue Problem is described in the form of:

$$Y_m(\eta;\xi)=\sin\left[\beta_m(\xi)\,(\eta-\varphi_0(\xi))\right], \tag{16a}$$

$$\beta_m(\xi)=\frac{m\,\pi}{(\varphi_1(\xi)-\varphi_0(\xi))}, \tag{16b}$$

where m is a positive integer. By the orthogonality, the norms are given by:

$$\int_{\varphi_0}^{\varphi_1}Y_m^2(\eta;\xi)\,\mathrm{d}\eta=\begin{cases}0\quad, & \text{if}\quad m\neq n\\ N_m\,, & \text{if}\quad m=n\end{cases} \tag{17}$$

$$N_m(\xi)=\frac{1}{2}\left[\varphi_1(\xi)-\varphi_0(\xi)\right] \tag{18}$$

After the definition of the transformation pair and solution of the Eigenvalue Problem, the transformation of the given formulation is accomplished by multiplying eq. (13a) by Y_m, integrating within $\varphi_0(\xi)\le\eta\le\varphi_1(\xi)$. The transformation procedure, gives after some simplification:

$$\gamma^2\,\frac{\mathrm{d}^2\overline{\psi}_m}{\mathrm{d}\xi^2}-\beta_m^2\,\overline{\psi}_m(\xi)-\gamma^2\sum_{n=1}^{\infty}A_{m,n}(\xi)\,\frac{\mathrm{d}\overline{\psi}_n}{\mathrm{d}\xi}-\gamma^2\sum_{n=1}^{\infty}B_{m,n}(\xi)\,\overline{\psi}_n=-\bar{C}_m(\xi)-\bar{G}_m(\xi), \tag{19}$$

In which the integral coefficients are given by:

$$A_{m,n}(\xi) = \frac{2}{N_n}\int_{\varphi_0}^{\varphi_1} Y_n \frac{\partial Y_m}{\partial \xi}\,\mathrm{d}\eta \tag{20a}$$

$$B_{m,n}(\xi) = \frac{1}{N_n}\int_{\varphi_0}^{\varphi_1} \left(2\frac{\partial Y_m}{\partial \xi}\frac{\partial Y_n}{\partial \xi} + Y_m \frac{\partial^2 Y_n}{\partial \xi^2}\right)\mathrm{d}\eta \tag{20b}$$

$$\bar{C}_m(\xi) = \int_{\varphi_0}^{\varphi_1} Y_m\,\mathrm{d}\eta \tag{20c}$$

$$\bar{G}_m(\xi) = \int_{\varphi_0}^{\varphi_1} G\,Y_m\,\mathrm{d}\eta \tag{20d}$$

To perform the solution of the transformed ODE, the boundary conditions must be transformed as well:

$$\overline{\psi}'_m(0) = \overline{\psi}_m(1) = 0, \tag{21}$$

Equations (19) and (21) constitute a boundary value problem composed of infinite coupled ODEs for $n = 1, 2, \ldots$. This system is truncated to a finite order and the considered problem solution is achieved by the routine **NDSolve**, available from the *Mathematica* platform (Wolfram, 2003).

5.1 Filter selection

A simpler version of the problem in question is obtained with the solution of the mathematical model of the flow in rectangular microchannels with $\phi = 0$, $\rho = 0$ and $\delta = 0$. With this solution, the system (19) becomes decoupled, and the analytical solution, using $F = 0$, is obtained:

$$\overline{\psi}(\xi) = \frac{\bar{C}_m}{\beta_m^2}\left[1 - \operatorname{sech}\left(\frac{\beta_m}{K}\right)\cosh\left(\frac{\beta_m}{K}\xi\right)\right] \tag{22}$$

For the rectangular microchannel solution, the previous expression is further simplified as $\bar{C}_m$ and β_m are independent of ξ.

Motivated by the familiar analytical solution for rectangular channels, a filter is proposed based on equation (22):

$$F(\xi,\eta) = \sum_{m=1}^{\infty} \frac{\bar{F}_m(\xi)\,Y_m(\eta;\xi)}{N_m} \tag{23}$$

in which $\bar{F}_m$ is given directly by equation (22); however, without considering the simplification $\phi = 0$, $\rho = 0$ and $\delta = 0$, which gives a distorted rectangular solution in the actual trapezoidal shape. With this filter, the term $\bar{G}_m$ is reduced to:

$$\bar{G}_m(\xi) = \gamma^2\,\bar{F}''_m(\xi) - \beta_m^2\,\bar{F}_m(\xi) \tag{24}$$

5.2 Recovery of the dimensionless velocity profile

System (19)-(21) is numerically solved, but the dimensionless velocity field must be recovered. Applying equations (8), (12), (14b) and (23), the dimensionless velocity $U(\xi,\eta)$ can be accomplished by the following equation:

$$U(\xi,\eta) = \frac{1}{\Gamma}\left(\sum_{m=1}^{\infty}\frac{\overline{\psi}_m(\xi)\,Y_m(\eta;\xi)}{N_m} + \sum_{m=1}^{\infty}\frac{\bar{F}_m(\xi)\,Y_m(\eta;\xi)}{N_m}\right), \tag{25}$$

As for the dimensionless pressure gradient, it can be calculated from:

$$\Gamma = \sum_{m=1}^{\infty}\int_0^1 \left(\overline{\psi}_m(\xi) + \bar{F}_m(\xi)\right)\frac{C_m(\xi)}{N_m(\xi)}\,\mathrm{d}\xi, \tag{26}$$

where the integrals are numerically calculated in the *Mathematica* system with the routine **NIntegrate**.

6. RESULTS AND DISCUSSION

The numerical results obtained with the current methodology are presented, with a preliminary comparison with the experimental data. Convergence analysis, graphic representations of the velocity profile and velocity values in different positions, pictured in figure 3, for different trapezoidal geometries, are included in the direct solution.

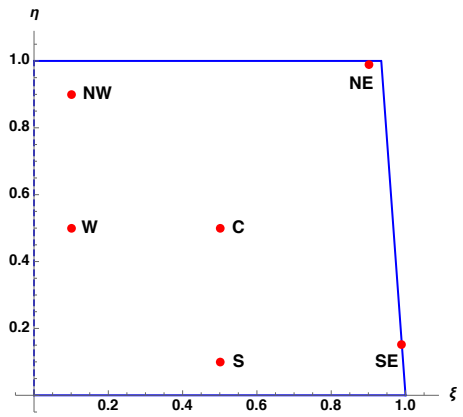

Figure 3: **Positions used in the convergence analysis.**

All the graphics and values represented were solved using $K = 2$ and ranging the angle ϕ, the dimensionless radius ρ and height δ. The first results are intended to verify the solution methodology and implementation by means of a convergence analysis of the numerical data. The velocity field is calculated for different truncation orders n_{max}, as shown in table 1, for a square duct. From table 1, a very good convergence is accomplished in most positions, with six converged

Table 1: **Poiseuille Number and dimensionless velocity values at different positions calculated for $\phi = 0$, $\rho = 0$ and $\delta = 0$ for different truncation orders.**

	$\phi = 0°$							
n_{max}	Γ	Po	U [**S**]	U [**C**]	U [**W**]	U [**NW**]	U [**N**]	U [**NE**]
5	0.0351312	0.0702624	2.09877	1.63143	0.0785580	0.0029516	0.0451711	0.0214511
10	0.0351426	0.0702852	2.09613	1.63180	0.0788061	0.0034506	0.0465779	0.0228602
20	0.0351441	0.0702882	2.09624	1.63138	0.0786265	0.0038506	0.0472723	0.0235571
30	0.0351442	0.0702884	2.09625	1.63143	0.0784163	0.0044394	0.0474892	0.0237746
40	0.0351443	0.0702886	2.09625	1.63142	0.0784020	0.0045298	0.0475869	0.0238724
50	0.0351443	0.0702886	2.09625	1.63141	0.0784096	0.0045787	0.0476375	0.0239230
60	0.0351443	0.0702886	2.09625	1.63141	0.0784058	0.0046057	0.0476652	0.0239506
70	0.0351443	0.0702886	2.09625	1.63141	0.0784081	0.0046205	0.0476802	0.0239657
80	0.0351443	0.0702886	2.09625	1.63141	0.0784066	0.0046283	0.0476881	0.0239735
90	0.0351443	0.0702886	2.09625	1.63141	0.0784077	0.0046317	0.0476915	0.0239770
100	0.0351443	0.0702886	2.09625	1.63141	0.0784069	0.0046326	0.0476924	0.0239779

digits being obtained with as low as 80 terms in some occasions. The convergence is worse near the walls φ, where only 3 fully converged digits are obtained for the presented 100 terms, which represents about 0.1% error. The worse convergence is still considered reasonable for many engineering applications.

The convergence analysis presented in areas closer to the walls can be explained by the presence of rounded corners. As evidenced before, the theoretical functions that characterize the domain are presented by discontinuities, that can influence in the convergence analysis near the walls.

The filter convergence $F(\xi, \eta)/\Gamma$ is presented in the following table for the trapezoidal microchannel with $K = 2$ and different sets of angles ϕ, radius ρ and height δ. As one can infer from these results, the convergence behavior is very similar to that observed in the previous case, with excellent convergence rates in positions away from the wall, which worsens at positions near the walls. However, the convergence analysis near the walls for the filter seems better than from the data generated in table 1. This fact is important during the consideration of the truncation order for the filter in the convergence analysis for the general solution $U(\xi, \eta)$.

A final comparison to be mentioned regards the experimental analysis, extracted from Puccetti *et al.* (2014), and the theoretical calculations provided by this study. The difference between experimental and theoretical approaches is investigated and displayed in figure 4. For all velocity profiles, the experimental dataset is the same. However, different

Table 2: **Poiseuille Number and the filter velocity values for different geometries and different truncation orders.**

n_{max}	Γ	Po	U [**W**]	U [**C**]	U [**NW**]	U [**S**]	U [**NE**]	U [**SE**]
			$\phi = 2°$, $\rho = 2 \times 10^{-1}$ e $\delta = 5/300$					
5	0.0338838	0.0700715	2.12679	1.67971	0.839808	0.609078	0.0218148	0.000412284
10	0.0339239	0.0701544	2.11863	1.67206	0.848580	0.621388	0.0242158	0.000463174
20	0.0339343	0.0701759	2.11611	1.66962	0.844134	0.618493	0.0264211	0.000515588
30	0.0339354	0.0701782	2.11629	1.66984	0.844927	0.618814	0.0271789	0.000535702
40	0.0339356	0.0701786	2.11621	1.66975	0.844632	0.618778	0.0275255	0.000545345
50	0.0339357	0.0701788	2.11622	1.66977	0.844762	0.618744	0.0277052	0.000550443
60	0.0339358	0.0701790	2.11621	1.66976	0.844690	0.618786	0.0278032	0.000553246
70	0.0339358	0.0701790	2.11621	1.66976	0.844732	0.618747	0.0278567	0.000554778
80	0.0339358	0.0701790	2.11621	1.66976	0.844704	0.618777	0.0278842	0.000555569
90	0.0339358	0.0701790	2.11621	1.66976	0.844722	0.618755	0.0278962	0.000555918
100	0.0339358	0.0701790	2.11621	1.66976	0.844710	0.618770	0.0278992	0.000556004
110	0.0339358	0.0701790	2.11621	1.66976	0.844719	0.618761	0.0278969	0.000555941
120	0.0339358	0.0701790	2.11621	1.66976	0.844712	0.618765	0.0278920	0.000555801
			$\phi = 5°$, $\rho = 10^{-2}$ e $\delta = 1/300$					
5	0.0342758	0.0741465	2.13159	1.67641	0.833590	0.665104	0.0153741	0.000168458
10	0.0343160	0.0742335	2.12333	1.66871	0.842912	0.675309	0.0167990	0.000184298
20	0.0343263	0.0742558	2.12071	1.66621	0.838504	0.671167	0.0180191	0.000198050
30	0.0343274	0.0742582	2.12094	1.66646	0.839295	0.671913	0.0184188	0.000202591
40	0.0343276	0.0742586	2.12082	1.66635	0.838999	0.671640	0.0185997	0.000204649
50	0.0343277	0.0742588	2.12086	1.66639	0.839132	0.671760	0.0186933	0.000205715
60	0.0343277	0.0742588	2.12084	1.66636	0.839057	0.671695	0.0187444	0.000206297
70	0.0343278	0.0742590	2.12085	1.66638	0.839101	0.671732	0.0187723	0.000206615
80	0.0343278	0.0742590	2.12084	1.66637	0.839072	0.671708	0.0187868	0.000206779
90	0.0343278	0.0742590	2.12084	1.66637	0.839091	0.671723	0.0187931	0.000206852
100	0.0343278	0.0742590	2.12084	1.66637	0.839077	0.671713	0.0187947	0.000206870
110	0.0343278	0.0742590	2.12084	1.66637	0.839087	0.671720	0.0187936	0.000206857
120	0.0343278	0.0742590	2.12084	1.66637	0.839079	0.671715	0.0187911	0.000206828

velocity field contours are calculated for different geometric parameters, in each figure.

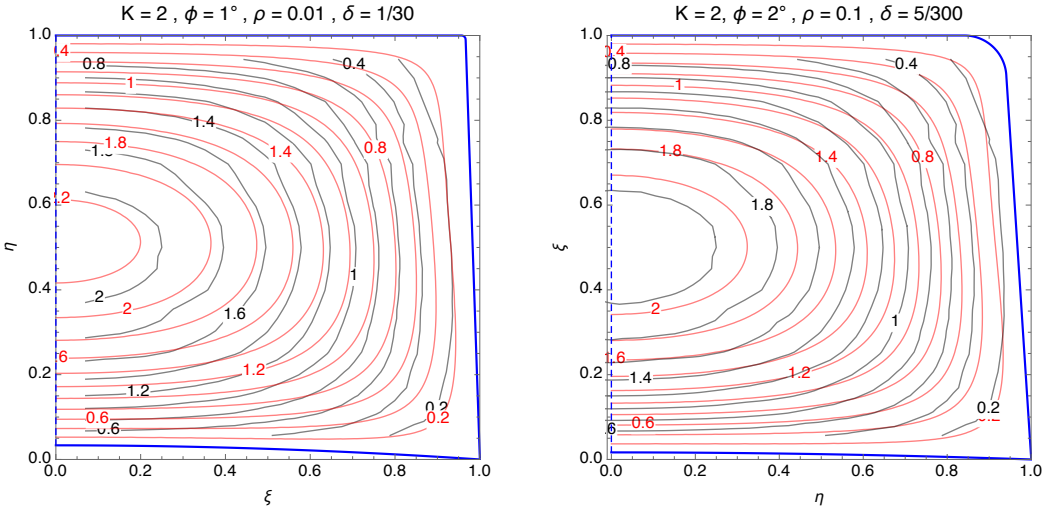

(a) $\phi = 1°$, $\rho = 10^{-2}$ and $\delta = 1/30$ (b) $\phi = 2°$, $\rho = 10^{-1}$ and $\delta = 5/300$

Figure 4: **Dimensionless velocity field for different configurations: experimental data (black), theoretical model (red).**

In further examination of the first figure, one can infer that the experimental velocity isolines are not in accordance with that obtained for a square microchannel cross-section. The center velocity field values seems higher with comparison of the experimental data. It can be concluded that the value of the height δ applied in the theoretical velocity in figure 4(a) is higher than the one expected.

When looking at figure 4(b), the experimental and theoretical curves display a clearly better agreement than seen in the previous plot. However, the theoretical curves near the wall are in better agreement with the first figure, which means

that the value of the angle is between 1° and 2°.

6.1 Normalized Root Mean Square Error (NRMSE)

Another way to establish the comparison between the experimental and the theoretical data of each cross-section geometric parameter is though the Normalized Root Mean Square Error (NRMSE). The values of this error for each case were calculated using the experimental data and the current formulation and are presented in table 3. As can be seen from

Table 3: **Normalized Root Mean Square Error (NRMSE) for imperfect trapezoidal geometries, at different η values.**

	NRMSE (%)		
η	$\phi = 1^\circ$ $\rho = 10^{-2}$ $\delta = 1/30$	$\phi = 2^\circ$ $\rho = 10^{-1}$ $\delta = 5/300$	$\phi = 5^\circ$ $\rho = 2 \times 10^{-1}$ $\delta = 1/300$
0.94	7.97	7.70	10.01
0.89	2.53	2.26	2.93
0.84	1.30	1.02	1.05
0.80	1.48	1.41	1.01
0.75	1.82	1.70	2.54
0.70	1.71	1.70	2.58
0.65	2.46	2.43	2.88
0.60	2.49	2.44	2.74
0.50	2.39	2.32	2.51
0.55	2.35	2.26	2.40
0.45	2.30	2.19	2.36
0.40	2.24	2.12	2.33
0.35	2.28	2.20	2.47
0.30	1.83	1.79	2.06
0.25	1.51	1.16	1.68
0.21	1.69	1.06	1.65
0.16	2.89	0.75	1.20
0.11	6.13	1.90	0.75
0.06	19.70	5.67	0.81
Total	5.44	2.82	3.09

these results, the error for the trapezoid angle of 2° is generally lower when compared with the other geometries in each considered position. In fact, the calculated NRMSE for 2° is lower for most presented η-value, with the exception of $\eta = 0.06$ and $\eta = 0.80$. This error can be reduce if different values of ρ and δ were incorporated in the trapezoid with $\phi = 2^\circ$.

A consideration inferred by the NRMSE analysis is that the error for the velocity field increases near the walls, reaching the maximum value of 7.70% for the closest micro-channel from the actual geometry. In contrast, the trapezoidal cross-section with $\phi = 1^\circ$ has a maximum NRMS Error of 7.97% in the upper boundary, while the value for 5° at the same position is 10.01%. In the lower boundary position ($\eta = 0.06$), the error is dependent of the value of δ, with a minimum value of 0.81% for $\delta = 1/300$.

The higher NRMS error near the microchannel walls can be explained by the values chosen to the radius of the rounded edges of the trapezoidal cross-section and the height δ in the numerical simulation. Nevertheless, in the central positions, the error is lower when compared to positions close to the walls, with values smaller than 2%.

As can be noted, the radius of the rounded corners and the height of the slightly curved surface have a major influence in the convergence and the agreement between experimental and theoretical datas. From the NRMS error, it can be said that the lower error near the walls is founded between $\delta = 1/300$ and $\delta = 5/300$. As for the radius, the influence is not only on the rounded corner, but in the center of the micro-channel. It can be difficult to estimate the actual radius in order to reduce NRMS Error, presented in table 3.

These results show, quantitatively, that the trapezoidal channel angle of 2° is in fact the case that is closer to the experimental data. The rest of the geometric parameters can be trick to find, but some mathematical tools can be applied. Inverse analysis techniques can be used in order to acquire the actual geometry profile.

7. SUMMARY AND CONCLUSIONS

This paper presented a hybrid methodology for solving fully-developed laminar fluid flow problems in a irregular microchannel generated by imperfections during manufacturing of rectangular microchannels. The geometry takes into account a tapered walls, which lead to a trapezoidal-like channels, with rounded corners. In addition, one of the channel walls – corresponding to a lid that is attached to the channels in the final fabrication stages – walls is curved inwards. These imperfections were parametrized in terms of three parameters: a trapezoid angle, a corner curvature radius, and a displacement at the center of the curved wall. The solution in terms of this irregular geometry was carried out in cartesian coordinates by employing the Generalized Integral Transform Technique, whose implementation was done in the Mathematica system. Also, a convergence analysis was carried out, showing that a relatively small amount of terms in the series is sufficient for producing a solution within acceptable errors, which can be further reduced if a higher precision is required. Following the convergence analysis, a parametric analysis was carried out to illustrate the influence that the imperfection parameters have on the velocity profile. At the current stage, the results need further refinement. Once this has been established, inverse analysis can be carried out for determining information regarding the channel geometry from experimental velocity data.

8. ACKNOWLEDGEMENTS

The authors would like to acknowledge the financial support provided by the Brazilian Government Funding Agencies, CAPES, CNPq, and FAPERJ.

9. REFERENCES

Abate, A.R., Lee, D., Holtze, C., Krummel, A., Doan, T. and Weitz, D., 2009. "Functionalized glass coating for pdms microfluidic devices". *Lab-on-a-Chip Technology: Fabrication and Microfluidics, Caister Academic Press*.

Aparecido, J. and Cotta, R., 1990. "Thermally developing laminar flow inside rectangular ducts". *International Journal of Heat and Mass Transfer*, Vol. 33, No. 2, pp. 341–347.

Cao, B., Chen, G.W. and Yuan, Q., 2005. "Fully developed laminar flow and heat transfer in smooth trapezoidal microchannel". *International communications in heat and mass transfer*, Vol. 32, No. 9, pp. 1211–1220.

Chalhub, D.J.N.M. and Sphaier, L.A., 2010. "Comparisons between gitt and fvm solutions for thermally developing flow in a rectangular duct". In *Proceedings of the 13th Brazilian Congress of Thermal Sciences and Engineering (ENCIT)*. ABCM, Uberlândia, MG, Brazil.

Cotta, R.M., 1993. *Integral transforms in computational heat and fluid flow*. 337 p. CRC Press, Boca Raton.

Florindo, I., Puccetti, G., Sphaier, L.A. and Morini, G.L., 2015. "Effects of fabrication imperfections on fully developed flow in rectangular micro-channels". *International Conference on Nanochannels, Microchannels, and Minichannels*.

Knupp, D.C., Naveira-Cotta, C.P. and Cotta, R.M., 2012. "Theoretical analysis of conjugated heat transfer with a single domain formulation and integral transforms". *International Communications in Heat and Mass Transfer*, Vol. 39, No. 3, pp. 355–362.

Knupp, D.C., Naveira-Cotta, C.P. and Cotta, R.M., 2013. "Conjugated convection-conduction analysis in microchannels with axial diffusion effects and a single domain formulation". *Journal of Heat Transfer*, Vol. 135, No. 9, p. 091401.

Kovacs, G.T., Maluf, N.I. and Petersen, K.E., 1998. "Bulk micromachining of silicon". *Proceedings of the IEEE*, Vol. 86, No. 8, pp. 1536–1551.

Lindquist, C. and Aparecido, J.B., 1999. "Laminar forced convection through rectangular ducts with uniform axial and peripheral heat flux". *Congresso Brasileiro de Engenharia Mecânica*.

McHale, J.P. and Garimella, S.V., 2010. "Heat transfer in trapezoidal microchannels of various aspect ratios". *International Journal of Heat and Mass Transfer*, Vol. 53, No. 1, pp. 365–375.

Naveira-Cotta, C.P., Cotta, R.M. and Orlande, H.R.B., 2010. "Inverse analysis of forced convection in micro-channels with slip flow via integral transforms and bayesian inference". *International Journal of Thermal Sciences*, Vol. 49, No. 6, pp. 879–888.

Niazmand, H., Renksizbulut, M. and Saeedi, E., 2008. "Developing slip-flow and heat transfer in trapezoidal microchannels". *International Journal of Heat and Mass Transfer*, Vol. 51, No. 25, pp. 6126–6135.

Petersen, K.E., 1982. "Silicon as a mechanical material". *Proceedings of the IEEE*, Vol. 70, No. 5, pp. 420–457.

Puccetti, G., Pulvirenti, B. and Morini, G.L., 2014. "Experimental determination of the 2d velocity laminar profile in glass microchannels using μpiv". *Energy Procedia*, Vol. 45, pp. 538–547.

Qu, W., Mala, G.M. and Li, D., 2000. "Heat transfer for water flow in trapezoidal silicon microchannels". *International Journal of Heat and Mass Transfer*, Vol. 43, No. 21, pp. 3925–3936.

Sheikhalipour, T., Abbassi, A. *et al.*, 2009. "Viscous dissipation effect in trapezoidal microchannels at constant heat flux". *Micro and Nano Flows Conference*.

Shokouhmand, H. and Jomeh, S., 2007. "Slip flow convection heat transfer in a rectangular microchannel with exponential wall heat flux." In *Proceedings of the World Congress on Engineering*. Citeseer, World Congress on Engineering (WCE), London, U.K., Vol. 2, pp. 1287–1292.

Sphaier, L.A., 2012. "Integral transform solution for heat transfer in parallel-plates micro-channels: Combined electroosmotic and pressure driven flows with isothermal walls". *International Communications in Heat and Mass Transfer*, Vol. 39, No. 6, pp. 769–775.

Weilin, Q., Mala, G.M. and Dongqing, L., 2000. "Pressure-driven water flows in trapezoidal silicon microchannels". *International Journal of Heat and Mass Transfer*, Vol. 43, No. 3, pp. 353–364.

Wolfram, S., 2003. *The Mathematica Book*. Wolfram Media/Cambridge University Press, New York/Champaign, IL, 5th edition.

Wu, H. and Cheng, P., 2003. "Friction factors in smooth trapezoidal silicon microchannels with different aspect ratios". *International Journal of Heat and Mass Transfer*, Vol. 46, No. 14, pp. 2519–2525.

10. RESPONSIBILITY NOTICE

The authors are the only responsible for the printed material included in this paper.